doi:10.1111/iej.13527

Contrast-enhanced nano-CT reveals soft dental tissues and cellular layers

T. Hildebrand[1,2], L. Nogueira[2], P. T. Sunde[3], D. Ørstavik[3], B. Glasmacher[1] & H. J. Haugen[2]

[1]Institute for Multiphase Processes, Leibniz University Hannover, Hannover, Germany; [2]Department of Biomaterials; and [3]Department of Endodontics, Institute of Clinical Dentistry, University of Oslo, Oslo, Norway

Abstract

Hildebrand T, Nogueira L, Sunde PT, Ørstavik D, Glasmacher B, Haugen HJ. Contrast-enhanced nano-CT reveals soft dental tissues and cellular layers. *International Endodontic Journal*, **54**, 1275–1288, 2021.

Aim To introduce a methodology designed to simultaneously visualize dental ultrastructures, including cellular and soft tissue components, by utilizing phosphotungstic acid (PTA) as a contrast-enhancement agent.

Methodology Sound third molars were collected from healthy human adults and fixed in 4% buffered paraformaldehyde. To evaluate the impact of PTA in concentrations of 0.3%, 0.7% and 1% on dental soft and hard tissues for CT imaging, cementum and dentine-pulp sections were cut, dehydrated and stained with immersion periods of 12, 24 h, 2 days or 5 days. The samples were scanned in a high-resolution nano-CT device using pixel sizes down to 0.5 μm to examine both the cementum and pulpal regions.

Results Dental cementum and periodontium as well as odontoblasts and predentine were made visible through PTA staining in high-resolution three-dimensional nano-CT scans. Different segments of the tooth required different staining protocols. The thickness of the cementum could be computed over the length of the tooth once it was made visible by the PTA-enhanced contrast, and the attached soft tissue components of the interior of the tooth could be shown on the dentine-pulp interface in greater detail. Three-dimensional illustrations allowed a histology-like visualization of the sections in all orientations with a single scan and easy sample preparation. The segmentation of the sigmoidal dentinal tubules and the surrounding dentine allowed a three-dimensional investigation and quantitative of the dentine composition, such as the tubular lumen or the ratio of the tubular lumen area to the dentinal surface.

Conclusion The staining protocol made it possible to visualize hard tissues along with cellular layers and soft tissues in teeth using a laboratory-based nano-CT technique. The protocol depended on both tissue type and size. This methodology offers enhanced possibilities for the concomitant visualization of soft and hard dental tissues.

Keywords: Cementum, contrast-enhanced nano-CT, dentin tubule, nano-CT, odontoblast.

Received 13 August 2020; accepted 5 April 2021

Introduction

Hard-tissue analyses with various computer tomographic techniques have proven to be of particular value in dentistry and endodontics (Peters *et al.* 2003, Silva *et al.* 2017, De-Deus *et al.* 2020). Micro-CT (Winter *et al.* 2005) and now nano-CT have found expanding applications in dental research (Haugen

Correspondence: H. J. Haugen, Department of Biomaterials, Institute of Clinical Dentistry, University of Oslo, PO Box 1109 Blindern, 0317 Oslo, Norway (e-mail: h.j.haugen@odont.uio.no).

et al. 2020). Whilst the complex structures of enamel, dentine and tooth cementum have been studied by 2D techniques for a long time, nano-CT technologies, with voxel sizes down to 300–500 nm, open new vistas for illustrating and understanding the details of dental hard tissues (Ahmed 2016, Kato *et al.* 2016).

Computed tomography allows nondestructive visualization of structures in the micrometre resolution range (Stauber & Müller 2008). Micro-CT is widely used in studies of mineralized dental tissues (Jung *et al.* 2005, Gandolfi *et al.* 2013, Ahmed *et al.* 2017, Johnsen *et al.* 2018). Biomaterials that previously could not be seen with X-rays can be made visible with contrast-enhancing agents (Bernemann *et al.* 2010, Crica *et al.* 2016). New X-ray developments are typically spearheaded at large-scale international synchrotron facilities (Hwu *et al.* 2017), and such technologies are rapidly adapted to laboratory-based equipment (Bultreys *et al.* 2016). Grating-based phase-contrast computed tomography (gbPC-CT) is one example; however, this technique is limited by a spatial resolution of 28 μm (Viermetz *et al.* 2018). In synchrotron phase-contrast micro-CT, the contrast originates from the phase shift of the X-ray beam passing through the material (Bravin *et al.* 2013). This phase shift enables imaging of tissue without X-ray contrast, such as the brain (Marinescu *et al.* 2013), cartilage (Coan *et al.* 2010) and osteocyte lacunae (Dierolf *et al.* 2010). However, these applications are not yet commercially available, being limited to a few specialized laboratories and synchrotron facilities that are costly and difficult to access (Giuliani *et al.* 2017).

Since a laboratory nano-CT system does not have all the features that a synchrotron facility can offer in terms of X-ray beam qualities (monochromatic beam, coherent beam, parallel beam, etc.), an easier approach for imaging soft tissues is to apply chemical staining to them, so that the contrast of softer structures can be enhanced due to a higher X-ray absorption in the stained tissue. The combination of nano-CT with specific staining protocols can take advantage of an increased resolution from the nano-CT, along with the ability to visualize both soft and hard tissue at the same time. Several methods use contrasting agents for staining soft tissues. Phosphotungstic acid (PTA) has been utilized as a standard histological technique for light and electron microscopy due to its capability to increase the contrast of soft (as distinguished from mineralized) tissues or different types of soft tissues. PTA attaches to collagen (Nemetschek *et al.* 1979) and various other proteins, and it is considered suitable for visualizing details in various soft connective tissues (Metscher 2009, Balint *et al.* 2016, Netzer *et al.* 2018).

CT techniques allow virtual sectioning of samples in any orientation (Singhal *et al.* 2013). Combined with morphometric measurements, structures can be fully quantified over volumes as well as areas. In this paper, a methodology that utilizes a laboratory nano-CT system to facilitate visualization in 3D X-ray images of cementum, periodontal ligaments, odontoblasts and hard tissues in freshly extracted teeth is presented.

Methods

Tooth specimens

Sound human third molars were collected from healthy human adults ($n = 10$). Written consent was obtained from all patients, and the project was approved by the Regional Ethical Committee (REK 2018/1404, Southeast Region, Norway). After extraction, the teeth were transferred to a sterile saline solution in 50 mL plastic vials at room temperature. The roots were cut off using a diamond saw on the day of extraction and immediately fixed in 7 mL of 4% buffered paraformaldehyde (PFA) solution in 10 mL centrifuge tubes overnight at room temperature. Further cementum and dentine-pulp specimen preparation were performed 24 h after fixation. All chemicals used were from VWR International® (Oslo, Norway).

Cementum section preparation

The fixed roots were rinsed in demineralized water using a wash bottle. The root of each sample was cut off with a diamond saw disc (NTI Superflex Diamond Discs; Kerr Dental, Brea, CA, USA) with an approximate length of 10 mm and transferred to Petri dishes containing ethanol with increasing concentrations (40%, 55% and 70%) at 30-min intervals. The dental tissues were then stained with 0.3%, 0.7% or 1.0% PTA solution (containing ten times the volume of the specimen) with immersion periods of 12, 24 h, 2 days or 5 days in 10 mL centrifuge tubes at room temperature. Before scanning, the samples were rinsed in 70% ethanol and mounted in an Eppendorf® tube (Eppendorf AG, Hamburg, Germany) containing a drop of 70%

ethanol in the bottom to assure a saturated environment and avoid shrinkage of the soft tissues during the scan. The samples were scanned in a nano-CT device, as detailed below. Control samples were submitted to the same fixation and ethanol dehydration methods but without any staining.

Dentine-pulp section preparation

After the removal of the dental crown by the diamond saw disc, cuboid samples of approximately $1 \times 1 \times 2$ mm^3 were cut from the paraformaldehyde-fixed dental roots containing the dentine-pulp interface with vertical, radial cuts along the transaxial plane. This was done manually using a 7 mm diamond saw disc with a disc thickness of 0.3 mm (NTI Superflex Diamond Discs; Kerr Dental). A horizontal cut by the saw disc isolated the cuboid samples from the dental root containing pulpal tissue. Cuts were performed under a magnifying lamp (3× magnification) and without water cooling. The samples were exposed to 70% ethanol by immersion in 40% and 55% ethanol for 3 min each in a Petri dish. They were then contrast-stained in 1 mL of 0.3%, 0.7% or 1.0% PTA solution for 12, 24 h, 2 days or 5 days in 1.5 mL micro-tubes at room temperature. The samples were rinsed in 70% ethanol, wrapped in Parafilm® M (Bemis Company Inc., Oshkosh, WI, USA) to avoid desiccation, and positioned in a polyamide tube with an inner diameter of 2 mm. The pulpal side of the tissue was left facing upwards for the nano-CT scan. Control samples were subjected to the same fixation and ethanol dehydration methods but without any staining.

Nano-computed tomography

All specimens were scanned in a nano-CT device (SkyScan 2211 Multiscale X-ray Nano-CT System; Bruker micro-CT, Kontich, Belgium) with a 20–190 kV tungsten X-ray source and a dual detection system: an 11-megapixel cooled 4032×2670 pixel CCD-camera and a 3-megapixel 1920×1536 pixel CMOS flat panel. Prepared roots for cementum analysis were scanned at 70 kV, 75 μA and 120 ms with a 0.5 mm Al filter placed between the source and the sample. The scans were taken over 180° with a rotation step of 0.3° and a voxel size of 8.0 μm using the flat panel detector. This led to a scan duration of 17 min for each sample. Cuboid samples of dentinal tissue containing the dentine-pulp interface were scanned at 60 kV, 320 μA and 1000 ms with a 0.125 mm Al filter over 360° with a rotation step of 0.47°, leading to a final voxel size of 0.5 μm. The scan duration for both the PTA-stained dentine-pulp and nonstained samples was about 2 h. Projections were reconstructed using the system-provided software, NRecon (version 1.7.4.6), and analysed with CTAn (Bruker micro-CT, version 1.18.4.0).

For quantification of the cementum thickness, a nonlocal means filter was applied to the data sets to denoise them (Buades *et al.* 2005). The thickness was computed by segmentation of the contrast-stained cementum in each transaxial section with a global lower grey threshold of 85 and an upper of 249. Further image improvement included the use of a series of image processing tools, such as closing and removal of speckles, to better clean the data sets. Finally, an automated 2D analysis of the average structure thickness in the segmented area of each section was performed (1182 sections in total) using CTAn (Bruker micro-CT). Greyscale shades were converted into colour by a computer algorithm for improved visualization of the soft tissue components.

For the visualization of soft tissues in the dentine cuboids, the same nonlocal means were applied, and the 3D images were rendered using Avizo® 9.0 (Thermo Fisher Scientific, Waltham, MA, USA; Table 1). The tubules were segmented using the Otsu method (Otsu 1979) and fine-tuned manually, then further quantified using Avizo® 9.0 (Thermo Fisher Scientific; Table 1). The quantified parameters included the tortuosity and diameter of the tubules. Tortuosity is the property of a curve being twisted and is defined as the arc-chord ratio: the ratio of the length of the curve and the distance between its ends (Epstein 1989). The diameter is calculated by taking the average of the minimum Feret diameters (Dražić *et al.* 2016) measured throughout each individual tubule, with a sampling over 100 directions. The Feret diameter is a measure of an object's size along a specified direction. It can be defined as the distance between the two parallel planes restricting the object perpendicular to that direction (Febbi *et al.* 2015). Furthermore, skewness is a measure of lack of symmetry, and kurtosis evaluates the degree of flatness of tubuli (Adeleye & Akanji 2018). All 3D illustrations were performed in CTVox (version 3.0, Bruker micro-CT) or Avizo® (Thermo Fisher Scientific) using computer-generated colours for specific ranges of attenuation in the sample. The Michelson contrast formula (Equation 1):

Table 1 3D characterization of tubules showing both the mean and median diameter as well as morphological parameters

3D Tubules characterization	
Parameter	Values
Mean diameter (μm)	5.0
Standard deviation (μm)	3.2
Median diameter (μm)	4.1
Kurtosis (-)	18.6
Skewness (-)	3.5

The skewness is a measure of symmetry inside the tubules, or more precisely, of the lack of symmetry. Since the skewness number is high, the tubule diameters are highly asymmetric. Kurtosis is a measure of the tubules' 3D volume, that is whether it is lighter or heavier in relation to a normal distribution. The high number shows that the kurtosis is leptokurtic, meaning that there is a large deviation from the smallest to the largest tubule diameter. The morphological parameters show that the tubules have irregular shapes.

$$C^M = (L_{\max} - L_{\min})/(L_{\max} + L_{\min}) \quad (1)$$

was used for contrast measurements (Michelson 1927), and the signal-to-noise ratio (SNR) was calculated as described by Mahesh (2011) with Equation 2 for the same regions of interest representatively for nonstained, 0.3% PTA stained (24 h), and 0.7% PTA stained (24 h) pulpal and dentine tissue.

$$\mathrm{SNR} = \frac{\mu}{\sigma} \quad (2)$$

Results

X-ray attenuation of dental cementum by PTA contrast staining

In the present setup, a subjectively optimal contrast was observed when 0.7% PTA in combination with 5 days of immersion was utilized. Lower PTA concentrations led to worse X-ray attenuation, whilst higher concentrations led to saturated X-ray attenuation. Shorter immersion periods also led to X-ray attenuation that was too low.

An increased X-ray attenuation of the dental cementum relative to the dentine was observed on the surface of the dental root (Fig. 1a–d) for 0.7% PTA over 5 days of immersion time. The enhanced contrast of the cementum relative to the dentine allowed for the analyses of cementum thickness along the root from the apex. By segmenting the contrast-stained tissue in the transaxial plane, as illustrated in Fig. 1a, two levels of thickness could be detected from the apex (Fig. 1e). The cervical portion of the root showed cementum as a 25 μm thick, sharply defined, opaque surface layer. In the apical portion of the root, the opaque surface layer increased in thickness to approximately 90 μm, and the ratio of the cementum-to-dentine area in the transaxial plane, excluding the dental pulp, increased from approximately 2% to 10% from the cervical towards the apical portion (Fig. 1f). In contrast to the cervical opaque surface layer, the apical contrast-stained tissue had a diffuse and interrupted appearance, as opposed to the sharply defined structure that surrounded the dentine. The transition from the coronal, homogenous cementum to the apical, thicker and more uneven cementum was abrupt.

Increased X-ray attenuation of pulpal tissue by PTA contrast staining

The subjectively optimal protocol for suitable X-ray attenuation was also found to be 0.7% PTA, the same as for the dental cementum; however, the better working immersion time was only 1 day. Figure 2a shows a cross section through an unstained sample with its grey values along the arrow in Fig. 2b. When a staining with 0.3% PTA for 24 h resulted in a very low enhancement of the region of interest (ROI; Fig. 2c, arrow), an immersion time of 48 h with 0.3% PTA led to a peak in grey value in the ROI, but also caused a gradient into the dentine (Fig. 2d, arrow). Regarding an appropriate contrast-stained tooth sample, the pulpal tissue and the dentine were defined by two distinguishable peaks in the grey value of a cross section through dentine and pulpal tissue (Fig. 2e, arrow). A longer immersion time resulted in oversaturation (Fig. 2f, arrow). With immersion times of 48 h, independent of whether the PTA concentration was 0.3% or 0.7%, the agent penetrated the dentine and caused a seamless increased X-ray attenuation, which rejected a visual separation of pulpal tissue and dentine. The quantification of contrast agreed with the choice for the staining concentration and time (Fig. S1a–d, Tables S1–S4). Cuboid pulp-dentine samples containing pulpal tissue were scanned with (Fig. 3d–f) and without (Fig. 3a–c) PTA contrast staining. Dentinal tubules were visible as channels perpendicular to the dentinal-pulp interface when using the favourable protocol. Figure 3d illustrates the stained layer in greyscale, whereas 3e and 3f have computer-generated colours to distinguish between cellular layers and dentine. A continuous cell layer was observed near the pulpal chamber, and cellular layers inside the tubules were visible

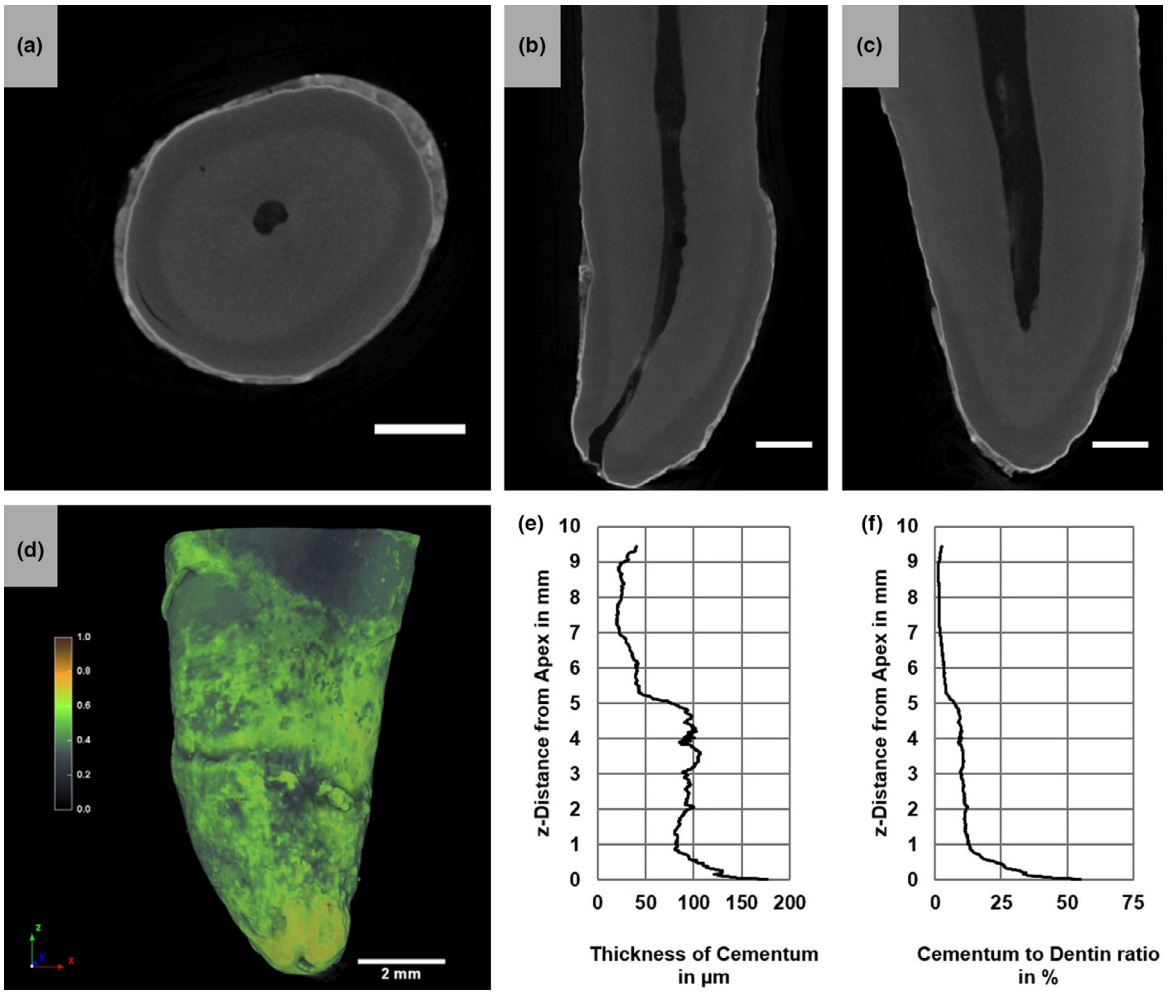

Figure 1 Staining of dental roots in PTA solution significantly increased the contrast of the surrounding layers in the nano-CT scan. The transaxial, sagittal and coronal sections of the CT scan (a–c) show the highest attenuation in the cementum (scale bar: 600 µm). The 3D model of reconstruction (d) illustrates the increase in the density of the contrast-stained tissue (green/orange) from the cervical towards the apical portion of the dental root. The colours show the normalized values of attenuation, where black is the lowest and orange the highest attenuation in the soft tissue. Analysis of cementum thickness versus height and cementum-to-dentine ratio (e–f) indicates an increase in tissue thickness in the apical portion.

through the contrast staining (Fig. 3e–f). Artefacts were seen in only a few regions: at the right-hand side of Fig. 3d, a slight detachment of the cellular layers is visible, caused by cutting with the diamond saw disc during the preparation of the tiny cuboid sample.

Visualization of organic layers within dental tubules

The PTA-stained 3D nano-CT images can be viewed as 2D images (Fig. 4a) and are similar to a regular histological image of a cross section of a tooth stained with haematoxylin and eosin (H&E; Fig. 4b; Saraga-Babić *et al.* 2007). Both images in Fig. 4 illustrate odontoblasts (labelled red) forming a pseudostratified layer of columnar cells at the dentine surface. Parallel dentine tubules containing odontoblastic processes extended through a narrow pale-stained zone of less calcified dentine matrix. Vertical holes and rings indicated by light blue colour define connections of the parallel tubules. The predentine is also visible in Fig. 4a with a thickness of approximately 20 µm,

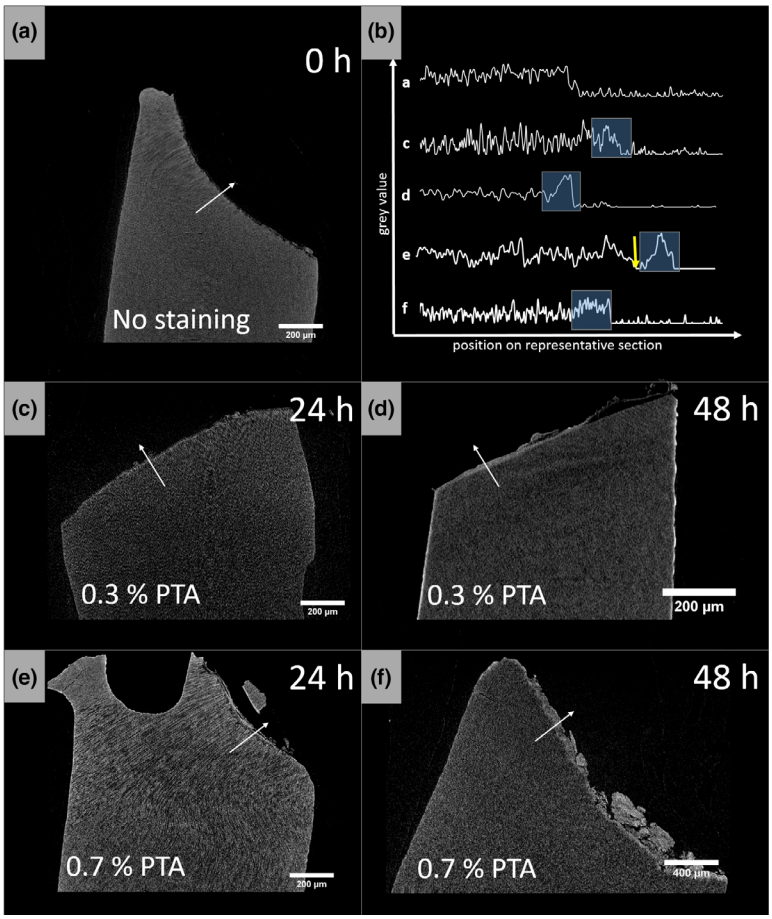

Figure 2 Dentine-pulp interface of untreated and PTA contrast-stained samples with different staining agent concentrations and immersion times (a, c–f) and resulting grey values of sections in the region of interest (b). Sagittal sections of nano-CT scans show that 0.3% PTA for 24 h created slightly increased attenuation on the interface (c) in contrast to the unstained sample (a). After 48 h of staining with 0.3% PTA, the soft tissue could not be completely separated from the dentine, caused by penetrating the staining agent into the dentine (d). The same effect was found for 0.7% PTA for 48 h (f). Staining with 0.7% PTA for 24 h caused a stained soft tissue layer on the interface without penetrating the dentine (e), illustrated by the step response in the grey value (b, yellow arrow), which enabled a histology-like illustration of the tissues (Fig. 4).

which corresponds to the dimensions described previously (Carrigan *et al.* 1984).

Entrances to the dentinal tubules can be observed in Fig. 5 as grey holes (Fig. 5a) pointing in a vertical direction to the pulpal dentine interphase. For improved visualization, the cellular components were filtered out by software (CTVox) for a catchy presentation of the underlying tubules. Due to the low attenuation of the dental tubules and high attenuation of the dentine, the structures could be highlighted, as shown in Fig. 5b. Tubules were visualized by highlighting specific ranges of attenuation of the sample in CTVox, leading to a three-dimensional illustration of the dental tubule network with diameters from 2 to 4 µm. At lower magnifications (Fig. 5c), the tubules exhibit a characteristic sigmoid curvature in the sagittal plane pointing towards the pulp (P) through the predentine (PD). A calcification front between the predentine and dentine (Fig. 5c) can also be observed, as in Fig. 3f; this was enabled by PTA staining.

Dentinal tubule 3D visualization

Figure 6a shows a 3D reconstructed cuboid sample of dentine, whereas b and c are virtual cuts of this 3D

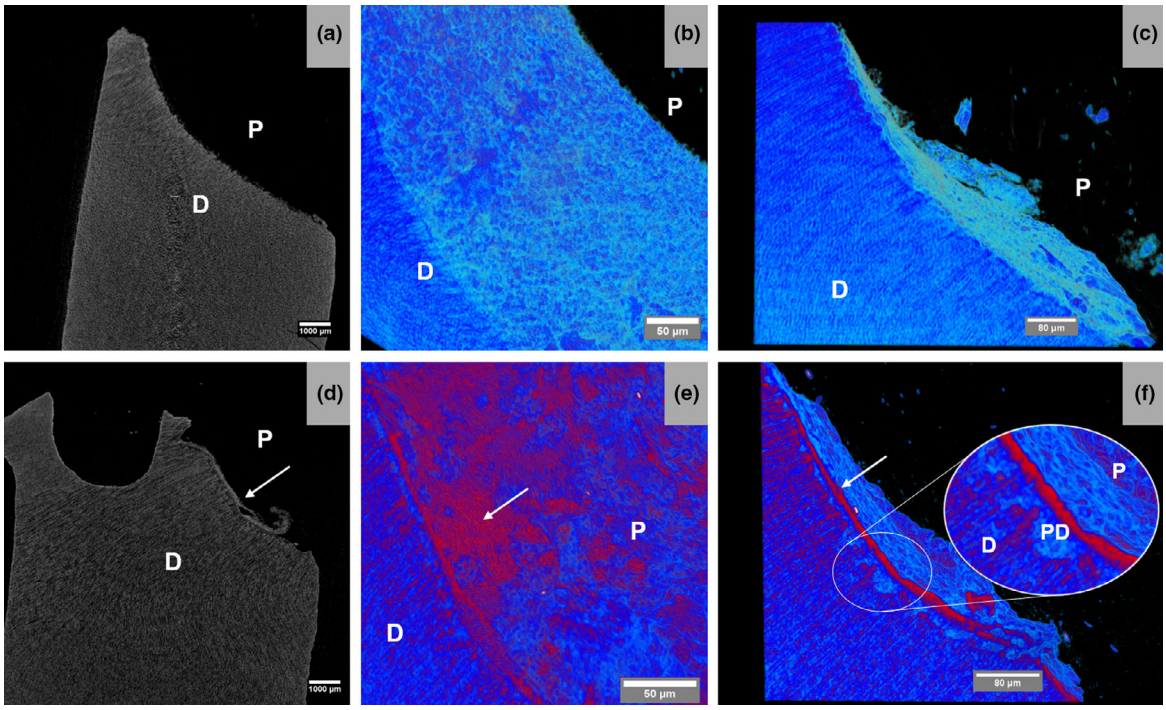

Figure 3 Dentine–pulp interface of untreated and PTA contrast-stained cuboid samples. A sagittal section of the nano-CT scan (a) and the 3D models of the reconstruction (b and c) show the untreated region of interest. A section (d) and the 3D reconstructions of the PTA-stained sample (e–f) enable visualization of the soft tissue (arrow) attached to the interface. 3D models use computer-generated colours, where the highest attenuation is indicated by red (odontoblasts), the lowest by black and a middle attenuation by light blue (arrow). P-pulp, D-dentine, PD-predentine.

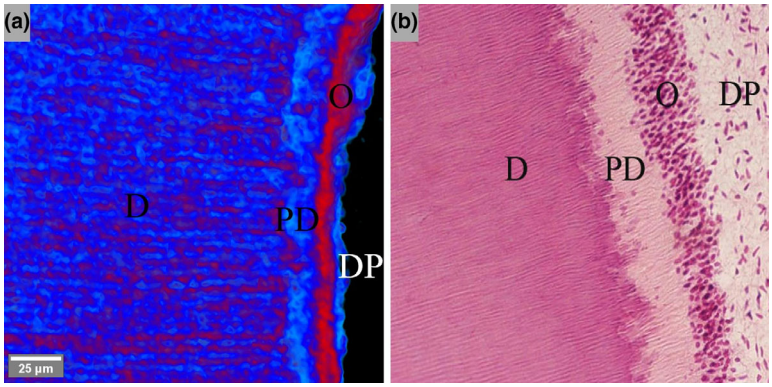

Figure 4 Comparison of a virtual slice of the 3D-generated nano-CT image stained with PTA (a) with a regular histological image of a cross section of a tooth stained with haematoxylin and eosin (H&E) at 40x magnification (b). Features visible in regular histology are also visible in the nano-CT scans. D-dentine, PD-predentine, O-Odontoblasts, DP-Dental pulp. Image (b) is reprinted with permission from Saraga-Babić *et al.* (2007).

image. The tubules' irregular shape and size were difficult to interpret when only shown in a 2D plane (Fig. 6b–c). Segmentation improved the visualization of the tubules, and their irregular structures, thicknesses and orientations were clearly visualized (Fig. 6d–f). This segmentation also allowed the

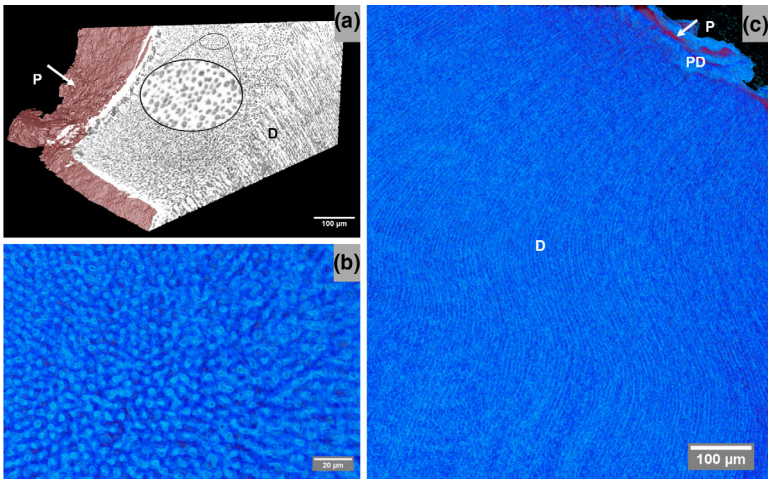

Figure 5 Visualization of the tubular network in a cuboid sample of a PTA-stained third molar. (a) Segmentation of the tubular network by CTAn allows investigation of the complex anatomical variation and tubular orientation in all dimensions. The cellular layer (red) stained by PTA was filtered out by software for improved visualization of the tubules' entry points. (b) Transversal cross section shows filtered tubules' lumen and several junctions of tubules can be observed. (c) A sagittal view on 3D reconstruction using computer-generated colours illustrates the characteristic S-shape of tubules pointing towards the pulp (P). A calcification front between the dentine (D) and predentine (PD) can be observed. White arrows show odontoblasts.

quantification of the tubules' local orientation, tortuosity and thickness (Fig. 6g–i), which varied in depths from the pupal space. The tubules had a mean diameter of 5.0 ± 3.2 µm and were larger in the dentine layer close to the pulp chamber. The diameter distribution can be seen in Fig. 7, where most of the diameter lies between 2.0 and 7.5 µm. Skewness (S_{sk} = 3.5) and kurtosis (K_u = 18.6) parameters confirmed the tubules' irregular shape and size (Table 1).

Discussion

The anatomical relationships between dental soft tissues and dentine and cementum are still not fully understood (Hesse *et al.* 2015). Traditionally, layers of acellular cementum have been studied by visual inspection of thin 2D sections under a microscope (Naji *et al.* 2016). Micro-CT or nano-CT do not provide enough contrast for 3D evaluation of cementum due to its low X-ray attenuation (Mavridou *et al.* 2016). The organic components of cellular cementum consist of up to 90% Type I collagen (Nanci 2017). PTA, which binds nonspecifically to collagen (Kerckhofs *et al.* 2018, Marchiori *et al.* 2019), increases the X-ray attenuation of the soft tissue, and has been investigated for collagen tracking in human and bovine knee joint cartilage (Nieminen *et al.* 2015). Here, the contrast agent PTA applied to dental tissues permits detailed analysis of soft tissues along with hard dental tissues in nano-CT scans.

The main difference between nano- and micro-CT lies in their voxel size. The voxel size for nano-CT is typically lower than 1 µm, and for micro-CT, typically over 2 µm (Kampschulte *et al.* 2016). However, even if a sample is scanned in a nano-CT, it does not automatically follow that the resolution will be in the submicrometre range. The final image resolution is usually assessed by the 10% modulation transfer function (MTF; Tjong *et al.* 2012). In the present study, two different voxel sizes were used: 8 µm when studying PTA-stained cementum and 0.5 µm when studying PTA-stained cuboids from the pulpal chamber. The calculated cementum thicknesses (25 and 90 µm) from the transaxial plane on PTA-stained dental roots were found to be comparable to histological measurements of the same structures (Chen & Liu 2014, Yamamoto *et al.* 2016); however, the thickness of the apical cementum layer was thinner (90 µm vs. 150–200 µm) than earlier reports. Cementum thickness depends on several clinical factors, including age (Azaz *et al.* 1974, Vishwakarma *et al.* 2014). Moreover, the staining process (via PTA) before scanning could have caused volumetric shrinkage, which has been reported previously when using PTA for other tissues (Buytaert *et al.* 2014). The cementum

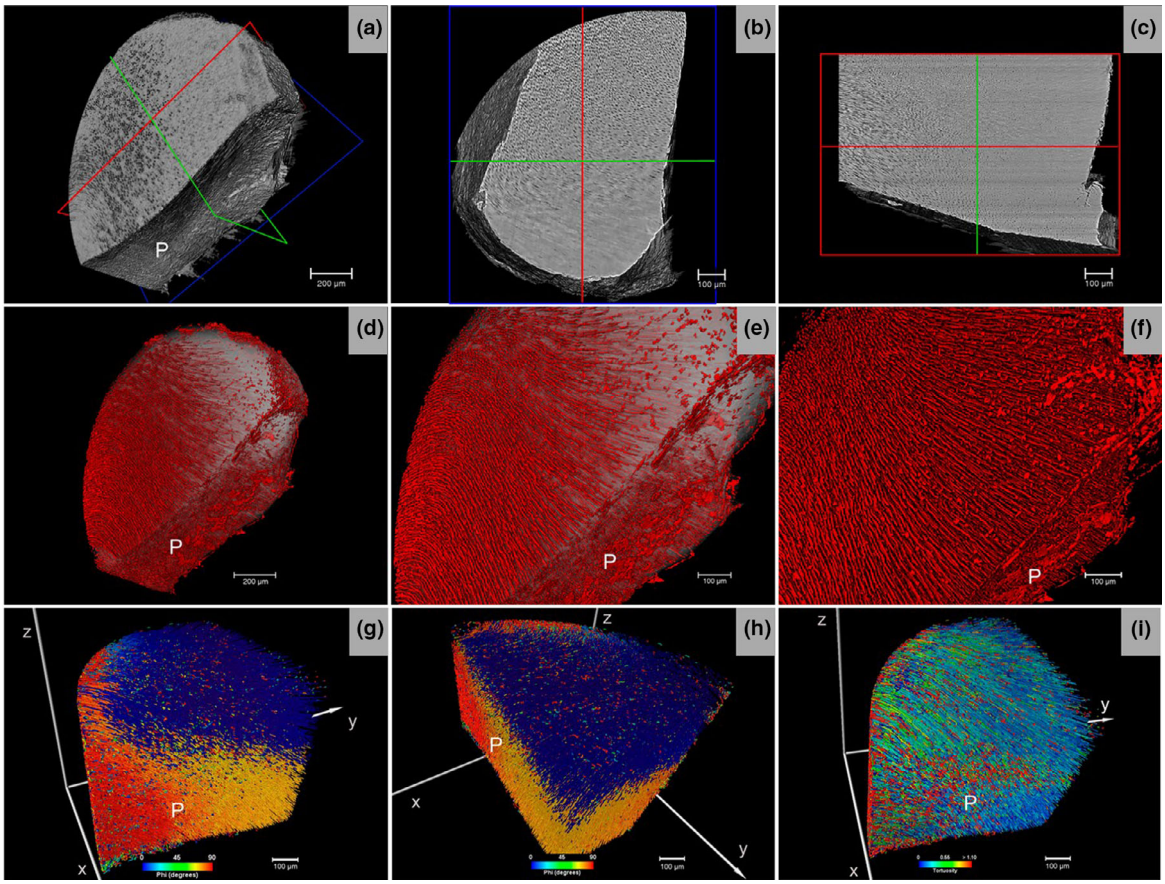

Figure 6 shows the 3D reconstructed cuboid sample of dentine. Images a, b and c show a virtual cut in the transversal and coronal planes from A. Tubule morphology is difficult to notice in the 2D plane (a, b and c). Images d, e and f show the highlighted tubule structures segmented in red. The tubules (red) are obvious, and the inclination and thickness of the tubules were observed to vary from the pulp chamber towards the dentine. The threshold selection used to image the tubules highlighted soft tissues unevenly at the tubules' entrance in the pulpal chamber (d–f). The high-resolution 3D data set with the staining allowed for tubule morphology quantification. Images g and h show the tubules' orientation from two different angles. Blue denotes 0° and red represents 90° of orientation difference (from the *x*-axis). Image i shows the tortuosity (a property of a curve being twisted, having many turns). Red means a high degree and blue a low degree of twistedness/tortuosity. P denotes the side of the pupal chamber. The cuboid's dimensions are about $1 \times 1 \times 1$ mm^3.

increased in thickness rapidly over a 1 mm distance towards the apex of the root. Also, the cementum-dentine ratio increased from 15% to more than 50%, indicating the transition to the overhanging cellular intrinsic fibre cementum (CIFC) at the root apex. The thickness of the CIFC without the transition zone had a height of 4.0 mm along the apical third. The results of contrast staining of the CIFC correspond well to previous studies on human premolars, where backscattered scanning electron micrographs were used to study CIFC from an apical to a coronal direction (Nanci & Bosshardt 2006).

The PTA-stained cuboids (approximately $1 \times 1 \times 2$ mm^3) provided information regarding the ultrastructure along the dentine-pulp interface. The pulp has an organic matrix with collagen types I and III (Chen & Liu 2014). The pulp tissue can also be stained with iodine-potassium iodide (Lugol's solution), which adds contrast to pulp tissue in micro-CT images and allows identification of remaining pulp tissues after endodontic treatment procedures (De-Deus *et al.* 2021). The present study revealed that PTA stains not only cellular cementum but also the cellular components of the pulp, and it increased the X-

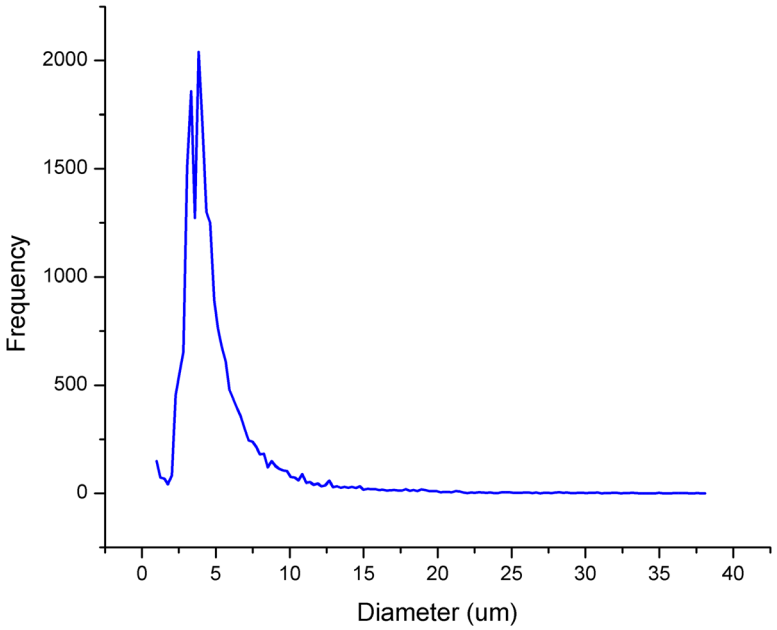

Figure 7 Diameter distribution of the dentinal tubules measured in 3D from nano-CT scans.

ray attenuation in these areas. The PTA-staining protocol depended on both dental tissue type and size, and it is likely that the PTA concentration and immersion time need to be adapted for each individual experiment. In the present study, PTA at a concentration of 0.7% to be suitable. However, the immersion time needed to be varied dependent on the tissue type and size of the specimen.

The predentine at the dentine-pulp interface was clearly visible in the nano-CT scan, as seen in Fig. 3d–f with the reference shown in Fig. 3a–c. The immersion time of the staining solution (24 h) may not have been enough for total penetration of the PTA through the predentine, as indicated by a non-homogenous representation of the predentine along the dentine-pulp junction (Fig. 2e). Odontoblasts were seen in the contrast-enhanced nano-CT images as clusters; however, individual cells were difficult to discern. Whilst it was demonstrated that the odontoblast processes could be labelled and identified (Fig. 3), the odontoblast cells themselves were difficult to observe as separate entities. Further work is necessary to differentially stain cellular structures such as membranes and organelles before nano-CT techniques can distinguish the individual cells in the dental soft tissues. Nevertheless, the resemblance to regular H&E staining (Fig. 4; Wan *et al.* 2015) demonstrates that contrast-enhanced nano-CT images are compatible with conventional histology and thus enable 3D histological evaluation of dental soft tissues. The development of user-independent analysis tools integrated with machine-learning image analysis may then permit the quantification of anatomical structures. Notably, contrast-enhanced nano-CT could provide evidence complementary to standard histology, but with the advantages of being less destructive and time-consuming, requiring no decalcification and allowing virtual tissue sectioning in any orientation. Conventional histology often requires decalcification, and tissue sectioning is destructive, typically along a single orientation plane (Nieminen *et al.* 2017).

Currently, histology remains an indispensable technique when studying dental tissue at microscopic scales for diagnostic and research purposes (Bancroft & Gamble 2008). Nieminen *et al.* stated that conventional histology has the following limitations: (i) destructiveness; (ii) sample-processing artefacts; (iii) nonrepresentation of spatial 3D structure and composition by the 2D tissue section; and (iv) the subjectivity of the outcome plane (Nieminen *et al.* 2017). Despite the developments made in 3D reconstruction techniques based on histological sections, such as semi-automated and automated section realignment, these techniques still have limitations. Contrast-

enhanced nano-CT techniques for the life sciences may overcome these limitations (Descamps *et al.* 2014, Minamino *et al.* 2015, Silva *et al.* 2015). One disadvantage of contrast-enhanced nano-CT is that the staining protocol needs to be fine-tuned for all sample types and sizes. Additionally, high-resolution nano-CT requires small sections and precise manual cutting in minimal dimensions, which can be challenging. Laser sectioning is now commercially available, although such equipment is expensive.

Dentinal tubules vary in morphology, number and size regarding their position in the root canal. Whilst the tubular lumen area decreases from the coronal to the apical portion, the intertubular area increases (Lo Giudice *et al.* 2015). The segmentation of the tubular network and remaining dentinal tissue allowed for a three-dimensional investigation of the dentine composition in the present study, including the tubular lumen and the ratio of the tubular lumen area to the dentinal surface. This ratio has been described as essential for developing materials that effectively bind to dentine (Mjør *et al.* 2001) and is typically assessed using scanning electron microscopy (SEM; Lo Giudice *et al.* 2015). 3D characterization of dentine tubules has been attempted previously; however, there are concerns regarding X-ray signal interferences (Boswell *et al.* 2013). High-resolution nano-CT scans with PTA staining enabled a comprehensive and descriptive analysis of the anatomical variation of dental tubules, including the noncalcified predentine. This may provide a better understanding of the relationships at the interfaces of the coronal, middle and apical dentine surfaces to pulpal and cemental tissues. The diameters of the tubules (Table 1) were comparable to those found by SEM investigations (Lopes *et al.* 2009) and, the nano-CT scans revealed the tubules' tortuous and irregular nature. Another advantage with nano-CT 3D imaging is the number of measurements that can be analysed when compared to conventional microscopy: here, more than 2000 images were analysed to obtain the data seen in Table 1. Obtaining a comparably large amount of measurement with conventional SEM and image analysis programs would have been very time-consuming.

The functions of cementocytes and their anatomical relationships in root cementum need further investigations. It has been speculated that they interconnect through cytoplasmic projections similar to osteocytes (Peyrin *et al.* 2014, Hesse *et al.* 2015); however, these features are not well documented for cementocytes (Zhao *et al.* 2016). On the other side of the dentine-cementum interface, the dentinal tubules housing the odontoblast processes end at or just beneath the junction of the two tissues. Here, the interdependence amongst the hard tissues of dentine, cementum and their cellular elements is still not fully understood (Papagerakis & Mitsiadis 2019). The present work demonstrates a methodical approach for characterization of soft as well as hard dental tissues and cellular relationships in three-dimensional freshly extracted teeth.

Conclusion

A staining protocol for visualization of dental ultrastructure using contrast-enhanced nano-CT technology is introduced. Hard and soft dental tissues were made visible in the same specimens with an X-ray imaging enhancement agent (PTA) and with laboratory nano-CT technology. The images obtained using nano-CT were similar to regular H&E staining of odontoblasts, which suggests that contrast-enhanced nano-CT images reflect what is seen with conventional histology. The suitable X-ray contrast depended on tissue type and volume in the proposed protocol; with appropriate adaptation, it can be used as a reference for future contrast-enhanced studies of 3D cellular structures in teeth. Most importantly, contrast-enhanced nano-CT scans provide 3D visualization within the same data set of the dental tissues and subsequently allow for spatial analyses, both descriptive and quantitative.

Acknowledgements

We hereby acknowledge Prof. Damir Sapunar, MD, PhD, Department of Anatomy, Histology and Embryology, School of Medicine, University of Split, for permission to reuse the histological image (Fig. 3A) from his project 'Virtual Medical School' (http://genom.mefst.hr/HistologyAtlas/).

Conflict of interest

The authors have stated explicitly that there are no conflicts of interest in connection with this article.

References

Adeleye JO, Akanji LT (2018) Pore-scale analyses of heterogeneity and representative elementary volume for unconventional shale rocks using statistical tools. *Journal*

of Petroleum Exploration and Production Technology **8**, 753–65.

Ahmed HM (2016) Nano-computed tomography: current and future perspectives. *Restorative Dentistry & Endodontics* **41**, 236–8.

Ahmed HMA, Versiani MA, De-Deus G, Dummer PMH (2017) A new system for classifying root and root canal morphology. *International Endodontic Journal* **50**, 761–70.

Azaz B, Ulmansky M, Moshev R, Sela J (1974) Correlation between age and thickness of cementum in impacted teeth. *Oral Surgery Oral Medicine Oral Pathology Oral Radiology and Endodontology* **38**, 691–4.

Balint R, Lowe T, Shearer T (2016) Optimal contrast agent staining of ligaments and tendons for X-ray computed tomography. *PLoS One* **11**, e0153552.

Bancroft JD, Gamble M (2008) *Theory and Practice of Histological Techniques*, 6th edn. Amsterdam, Netherlands: Elsevier Health Sciences.

Bernemann I, Manuchehrabadi N, Spindler R *et al.* (2010) Diffusion of dimethyl sulfoxide in tissue engineered collagen scaffolds visualized by computer tomography. *Cryo Letters* **31**, 493–503.

Boswell H, Merkle A, Gelb J *et al.* (2013) 3D characterisation of the occlusion of dentine tubules. *Microscopy and Microanalysis* **19**, 648–9.

Bravin A, Coan P, Suortti P (2013) X-ray phase-contrast imaging: from pre-clinical applications towards clinics. *Physics in Medicine and Biology* **58**, R1–35.

Buades A, Coll B, Morel J-M (2005) A non-local algorithm for image denoising. In: Schmid, C, Soatto, S, Tomasi, C, eds. *2005 IEEE Computer Society Conference on Computer Vision and Pattern Recognition (CVPR'05)*. San Diego, CA: IEEE, pp. 60–5.

Bultreys T, Boone MA, Boone MN *et al.* (2016) Fast laboratory-based micro-computed tomography for pore-scale research: illustrative experiments and perspectives on the future. *Advances in Water Resources* **95**, 341–51.

Buytaert J, Goyens J, De Greef D, Aerts P, Dirckx J (2014) Volume shrinkage of bone, brain and muscle tissue in sample preparation for micro-CT and light sheet fluorescence microscopy (LSFM). *Microscopy and Microanalysis* **20**, 1208–17.

Carrigan PJ, Morse DR, Furst ML, Sinai IH (1984) A scanning electron microscopic evaluation of human dentinal tubules according to age and location. *Journal of Endodontics* **10**, 359–63.

Chen H, Liu Y (2014) *Teeth advanced ceramics for dentistry*. Amsterdam, Netherlands: Elsevier, pp. 5–21.

Coan P, Bamberg F, Diemoz PC *et al.* (2010) Characterization of osteoarthritic and normal human patella cartilage by computed tomography X-ray phase-contrast imaging: a feasibility study. *Investigative Radiology* **45**, 437–44.

Crica LE, Wengenroth J, Tiainen H, Ionita M, Haugen HJ (2016) Enhanced X-ray absorption for micro-CT analysis of low density polymers. *Journal of Biomaterials Science, Polymer Edition* **27**, 805–23.

De-Deus G, Belladonna F, Cavalcante D *et al.* (2021) Contrast-enhanced micro-CT to assess dental pulp tissue debridement in root canals of extracted teeth: a series of cascading experiments towards method validation. *International Endodontic Journal* **54**, 279–93.

De-Deus G, Simoes-Carvalho M, Belladonna FG *et al.* (2020) Creation of well-balanced experimental groups for comparative endodontic laboratory studies: a new proposal based on micro-CT and in silico methods. *International Endodontic Journal* **53**, 974–85.

Descamps E, Sochacka A, De Kegel B, Van Loo D, Van Hoorebeke L, Adriaens D (2014) Soft tissue discrimination with contrast agents using micro-CT scanning. *Belgian Journal of Zoology* **144**, 20–40.

Dierolf M, Menzel A, Thibault P *et al.* (2010) Ptychographic X-ray computed tomography at the nanoscale. *Nature* **467**, 436–9.

Dražić S, Sladoje N, Lindblad J (2016) Estimation of Feret's diameter from pixel coverage representation of a shape. *Pattern Recognition Letters* **80**, 37–45.

Epstein N (1989) On tortuosity and the tortuosity factor in flow and diffusion through porous media. *Chemical Engineering Science* **44**, 777–9.

Febbi P, Menesatti P, Costa C, Pari L, Cecchini M (2015) Automated determination of poplar chip size distribution based on combined image and multivariate analyses. *Biomass & Bioenergy* **73**, 1–10.

Gandolfi MG, Parrilli AP, Fini M, Prati C, Dummer PMH (2013) 3D micro-CT analysis of the interface voids associated with Thermafil root fillings used with AH Plus or a flowable MTA sealer. *International Endodontic Journal* **46**, 253–63.

Giuliani A, Mazzoni S, Mele L, Liccardo D, Tromba G, Langer M (2017) Synchrotron phase tomography: an emerging imaging method for microvessel detection in engineered bone of craniofacial districts. *Frontiers in Physiology* **8**, 769.

Haugen HJ, Qasim SB, Matinlinna JP, Vallittu P, Nogueira LP (2020) Nano-CT as tool for characterization of dental resin composites. *Scientific Reports* **10**, 15520.

Hesse B, Varga P, Langer M *et al.* (2015) Canalicular network morphology is the major determinant of the spatial distribution of mass density in human bone tissue: evidence by means of synchrotron radiation phase-contrast nano-CT. *Journal of Bone and Mineral Research* **30**, 346–56.

Hwu Y, Margaritondo G, Chiang AS (2017) Q&A: why use synchrotron X-ray tomography for multi-scale connectome mapping? *BMC Biology* **15**, 122.

Johnsen GF, Sunde PT, Haugen HJ (2018) Validation of contralateral premolars as the substrate for endodontic comparison studies. *International Endodontic Journal* **51**, 942–51.

Jung M, Lommel D, Klimek J (2005) The imaging of root canal obturation using micro-CT. *International Endodontic Journal* **38**, 617–26.

Kampschulte M, Langheinirch A, Sender J *et al.* (2016) Nano-computed tomography: technique and applications. *Fortschritte auf dem Gebiet der Röntgenstrahlen und der bildgebenden Verfahren* **188**, 146–54.

Kato A, Ziegler A, Utsumi M, Ohno K, Takeichi T (2016) Three-dimensional imaging of internal tooth structures: applications in dental education. *Journal of Oral Biosciences* **58**, 100–11.

Kerckhofs G, Stegen S, van Gastel N *et al.* (2018) Simultaneous three-dimensional visualization of mineralized and soft skeletal tissues by a novel microCT contrast agent with polyoxometalate structure. *Biomaterials* **159**, 1–12.

Lo Giudice G, Cutroneo G, Centofanti A *et al.* (2015) Dentin morphology of root canal surface: a quantitative evaluation based on a scanning electronic microscopy study. *Biomedical Materials* **2015**, 164065.

Lopes MB, Sinhoreti MA, Gonini Júnior A, Consani S, Mccabe JF (2009) Comparative study of tubular diameter and quantity for human and bovine dentin at different depths. *Brazilian Dental Journal* **20**, 279–83.

Mahesh M (2011) Image quality. In: Bushberg JT, Boone JM, eds. *The Essential Physics of Medical Imaging*, 3rd edn. Philadelphia, PA: Lippincott Williams & Wilkins, pp. 60–96.

Marchiori G, Parrilli A, Sancisi N *et al.* (2019) Integration of micro-CT and uniaxial loading to analyse the evolution of 3D microstructure under increasing strain: application to the anterior cruciate ligament. *Materials Today-Proceedings* **7**, 501–7.

Marinescu M, Langer M, Durand A *et al.* (2013) Synchrotron radiation X-ray phase micro-computed tomography as a new method to detect iron oxide nanoparticles in the brain. *Molecular Imaging and Biology* **15**, 552–9.

Mavridou A, Pyka G, Kerckhofs G *et al.* (2016) A novel multimodular methodology to investigate external cervical tooth resorption. *International Endodontic Journal* **49**, 287–300.

Metscher BD (2009) MicroCT for developmental biology: a versatile tool for high-contrast 3D imaging at histological resolutions. *Developmental Dynamics* **238**, 632–40.

Michelson A (1927) Studies in optics. In: Michelson A, ed. *Harvey B. Plotnick Collection of the History of Quantum Mechanics and the Theory of Relativity*. Chicago, IL: The University of Chicago Press.

Minamino T, Mine A, Matsumoto M *et al.* (2015) Nondestructive observation of teeth post core-space using optical coherence tomography: comparison with microcomputed tomography and live images. *Journal of Biomedical Optics* **20**, 107001.

Mjør IA, Smith MR, Ferrari M, Mannocci F (2001) The structure of dentine in the apical region of human teeth. *International Endodontic Journal* **34**, 346–53.

Naji S, Colard T, Blondiaux J, Bertrand B, d'Incau E, Bocquet-Appel J-P (2016) Cementochronology, to cut or not to cut? *International Journal of Paleopathology* **15**, 113–9.

Nanci A (2017) *Ten Cate's Oral Histology-e-book: Development, Structure, and Function*, 9th edn. Amsterdam, Netherlands: Elsevier Health Sciences.

Nanci A, Bosshardt DD (2006) Structure of periodontal tissues in health and disease. *Periodontology 2000* **40**, 11–28.

Nemetschek T, Riedl H, Jonak R (1979) Topochemistry of the binding of phosphotungstic acid to collagen. *Journal of Molecular Biology* **133**, 67–83.

Netzer C, Scharen S, Geurts J (2018) Phosphotungstic acid-enhanced micro computed tomography for three-dimensional visualization and analysis of collagen distribution in human osteochondral tissues. *Osteoarthritis and Cartilage* **26**, S432.

Nieminen H, Gahunia H, Pritzker K *et al.* (2017) 3D histopathological grading of osteochondral tissue using contrast-enhanced micro-computed tomography. *Osteoarthritis Cartilage* **25**, 1680–9.

Nieminen H, Ylitalo T, Karhula S *et al.* (2015) Determining collagen distribution in articular cartilage using contrast-enhanced micro-computed tomography. *Osteoarthritis Cartilage* **23**, 1613–21.

Otsu N (1979) A threshold selection method from gray-level histograms. *IEEE Transactions on Systems, Man, and Cybernetics* **9**, 62–6.

Papagerakis P, Mitsiadis T (2019) Development and structure of teeth and periodontal teeth. In: Bilezikian JP, ed. *Primer on the Metabolic Bone Diseases and Disorders of Mineral Metabolism*. Hoboken, USA: Wiley Blackwell, p. 901.

Peters OA, Peters CI, Schonenberger K, Barbakow F (2003) ProTaper rotary root canal preparation: effects of canal anatomy on final shape analysed by micro CT. *International Endodontic Journal* **36**, 86–92.

Peyrin F, Dong P, Pacureanu A, Langer M (2014) Micro- and nano-CT for the study of bone ultrastructure. *Current Osteoporosis Reports* **12**, 465–74.

Saraga-Babić M, Sapunar D, Puljak L, Vukojević K, Lovrić Kojundžić S (2007) *Histology Atlas*. Virtual Medical School, University of Split, Croatia. http://genom.mefst.hr/HistologyAtlas/ (accessed on 3 April 2021).

Silva E, Perez R, Valentim R *et al.* (2017) Dissolution, dislocation and dimensional changes of endodontic sealers after a solubility challenge: a micro-CT approach. *International Endodontic Journal* **50**, 407–14.

Silva JM, Zanette I, Noël PB, Cardoso MB, Kimm MA, Pfeiffer F (2015) Three-dimensional non-destructive soft-tissue visualization with X-ray staining micro-tomography. *Scientific Reports* **5**, 1–7.

Singhal A, Grande JC, Zhou Y (2013) Micro/nano-CT for visualization of internal structures. *Microscopy Today* **21**, 16–22.

Stauber M, Müller R (2008) Micro-computed tomography: a method for the non-destructive evaluation of the three-dimensional structure of biological specimens. In: Westendorf J, ed. *Osteoporosis*. Berlin, Germany: Springer, pp. 273–92.

Tjong W, Kazakia GJ, Burghardt AJ, Majumdar S (2012) The effect of voxel size on high-resolution peripheral computed tomography measurements of trabecular and cortical bone microstructure. *Medical Physics* **39**, 1893–903.

Viermetz M, Birnbacher L, Willner M, Achterhold K, Pfeiffer F, Herzen J (2018) High resolution laboratory grating-based X-ray phase-contrast CT. *Scientific Reports* **8**, 15884.

Vishwakarma A, Sharpe P, Shi S, Ramalingam M (2014) *Stem Cell Biology and Tissue Engineering in Dental Sciences*. Cambridge, MA: Academic Press.

Wan L, Lu HB, Xuan DY, Yan YX, Zhang JC (2015) Histological changes within dental pulps in teeth with moderate-to-severe chronic periodontitis. *International Endodontic Journal* **48**, 95–102.

Winter AA, Pollack AS, Frommer HH, Koenig L (2005) Cone beam volumetric tomography vs. medical CT scanners. *New York State Dental Journal* **71**, 28–33.

Yamamoto T, Hasegawa T, Yamamoto T, Hongo H, Amizuka N (2016) Histology of human cementum: its structure, function, and development. *Japanese Dental Science Review* **52**, 63–74.

Zhao N, Foster BL, Bonewald LF (2016) The cementocyte-an osteocyte relative? *Journal of Dental Research* **95**, 734–41.

Supporting Information

Additional Supporting Information may be found in the online version of this article:

Figure S1. Selection of regions for determination of contrast and signal-to-noise ratio.

Table S1. Grey values measured at the different ROIs for the 0.7% PTA stained sample (24 h), the 0.3% PTA stained sample (24 h), and the nonstained sample.

Table S2. Results for the contrast (Michelson) and SNR of the 3 tested groups.

